International Journal of Nanomedicine

Dovepress
open access to scientific and medical research

Open Access Full Text Article

ORIGINAL RESEARCH

Mesoporous Silicon with Strontium-Powered Poly (Lactic-Co-Glycolic acid)/Gelatin-Based Dressings Facilitate Skin Tissue Repair

Naijing Li[1,*], Weiying Zhang[2,*], Siyuan Wu[3,*], Muhammad Shafiq[4], Peihan Xie[3], Lixiang Zhang[5], Shichao Jiang[3], Yue Bi[1]

[1]Department of Orthopedic Oncology, Yantai Shan Hospital, Yantai, People's Republic of China; [2]Health Management Center, Shandong Provincial Hospital Affiliated to Shandong First Medical University, Jinan, People's Republic of China; [3]Department of Orthopedics, Shandong Provincial Hospital Affiliated to Shandong First Medical University, Jinan, People's Republic of China; [4]Innovation Center of Nanomedicines, Kawasaki Institute of Industrial Promotion, Kawasaki, Japan; [5]Department of Health Management, Characteristic Medical Center of Chinese People's Armed Police Force, Tianjin, People's Republic of China

*These authors contributed equally to this work

Correspondence: Yue Bi; Shichao Jiang, Email dr_yuebi@126.com; mailjsc@163.com

Purpose: Functional inorganic nanomaterials (NMs) are widely exploited as bioactive materials and drug depots. The lack of a stable form of application of NMs at the site of skin injury, may impede the removal of the debridement, elevate pH, induce tissue toxicity, and limit their use in skin repair. This necessitates the advent of innovative wound dressings that overcome the above limitations. The overarching objective of this study was to exploit strontium-doped mesoporous silicon particles (PSiSr) to impart multifunctionality to poly(lactic-co-glycolic acid)/gelatin (PG)-based fibrous dressings (PG@PSiSr) for excisional wound management.

Methods: Mesoporous silicon particles (PSi) and PSiSr were synthesized using a chemo-synthetic approach. Both PSi and PSiSr were incorporated into PG fibers using electrospinning. A series of structure, morphology, pore size distribution, and cumulative pH studies on the PG@PSi and PG@PSiSr membranes were performed. Cytocompatibility, hemocompatibility, transwell migration, scratch wound healing, and delineated angiogenic properties of these composite dressings were tested in vitro. The biocompatibility of composite dressings in vivo was assessed by a subcutaneous implantation model of rats, while their potential for wound healing was discerned by implantation in a full-thickness excisional defect model of rats.

Results: The PG@PSiSr membranes can afford the sustained release of silicon ions (Si^{4+}) and strontium ions (Sr^{2+}) for up to 192 h as well as remarkably promote human umbilical vein endothelial cells (HUVECs) and NIH-3T3 fibroblasts migration. The PG@PSiSr membranes also showed better cytocompatibility, hemocompatibility, and significant formation of tubule-like networks of HUVECs in vitro. Moreover, PG@PSiSr membranes also facilitated the infiltration of host cells and promoted the deposition of collagen while reducing the accumulation of inflammatory cells in a subcutaneous implantation model in rats as assessed for up to day 14. Further evaluation of membranes transplanted in a full-thickness excisional wound model in rats showed rapid wound closure (PG@SiSr vs control, 96.1% vs 71.7%), re-epithelialization, and less inflammatory response alongside skin appendages formation (eg, blood vessels, glands, hair follicles, etc.).

Conclusion: To sum up, we successfully fabricated PSiSr particles and prepared PG@PSiSr dressings using electrospinning. The PSiSr-mediated release of therapeutic ions, such as Si^{4+} and Sr^{2+}, may improve the functionality of PLGA/Gel dressings for an effective wound repair, which may also have implications for the other soft tissue repair disciplines.

Keywords: electrospinning, nanofiber membrane, wound healing, mesoporous silicon, strontium

Introduction

Skin, as the first line of the defense to various toxins and pathogens, protects the underneath tissues from an excessive loss of the moisture as well as external insults. While the minute skin defects can be repaired by the natural healing

Received: 17 January 2024
Accepted: 22 May 2024
Published: 24 June 2024

mechanism of the body, chronic skin injuries, such as diabetic foot ulcers and burns may not be healed with full biofunctions (eg, hair follicles, sweat glands, appropriate mechanical strength, etc.). An incomplete wound regeneration along with scar tissue formation may pose serious complications for patients, thereby increasing healthcare burdens and impairing the quality of life (QOL).[1] Moreover, acute extensive trauma or chronic wounds may also perturb skin repair.[2] Artificial skin equivalents and tissue-engineered wound dressings may leverage a moist and a breathable environment and induce tissue repair. Meanwhile, tissue-engineered scaffolds with hemostasis, pro-tissue regeneration, or validated regulatory components, including particles, nanofibers, hydrogels, and aerogels could meet the characteristics of different wounds, which have been widely applied for wound healing.[3]

Functional inorganic nanomaterials (NMs), such as mesoporous silicon (PSi) with appropriate pore size, adjustable degradation rate, and spatiotemporal drug release, are widely exploited as bioactive materials and drug depots. These PSi particles may also have prospects for wound regeneration.[4] Moreover, the PSi may act as a depot for the sustained release of therapeutics and biologics owing to its porosity. The PSi has been intensively used as a vehicle for the sustained release of therapeutics with minimal inflammatory response.[5] The PSi could support cell proliferation as well as encourage de novo production of blood vessels plausibly by controllably furnishing therapeutic silicon ions (Si^{4+}) in the physiological microenvironment.[6] The strontium ions (Sr^{2+}) have been shown to promote bone repair.[7] Based on these advantages, we surmised that the Sr could be incorporated into PSi to afford strontium-loaded mesoporous silicon particles (PSiSr). However, owing to the biodegradability of mesoporous strontium particles, they cannot be directly used for skin repair. Besides, due to the lack of a stable application form at the skin injury site, PSiSr may impede the removal of the debridement, elevate pH, and possibly induce tissue toxicity.[1]

Electrospun fibers are widely used as scaffolds for in vitro cell culture as well as for in vivo transplantation. Thanks to their extracellular matrix (ECM)-mimetic structure as well as sufficient porosity, the latter may promote the diffusion of oxygen as well as the transport of nutrients.[8,9] Electrospun fibers have been widely used as depots for the controlled release of therapeutics, biologics, proteins, and growth factors (GFs) for various tissue engineering (TE) disciplines.[2] Consequently, the encapsulation of mesoporous PSi and PSiSr particles into electrospun fibers is expected to play an important role for the sustained and controlled release of therapeutics, while also overcoming inherent limitations associated with their direct implantation of these inorganic NMs at the injury site.[10]

We prepared PSi and PSiSr using a chemo-synthesis method and incorporated them into poly(lactic-co-glycolic acid)/Gelatin (PLGA/Gel, PG) fibers using electrospinning. The PG fibers are widely studied as wound dressings owing to the tunable degradability and good mechanical strength of PLGA alongside sufficient biocompatibility, cell recognizability, and biodegradability of the Gel.[10]

In this study, the biocompatibility and biofunction of composite dressings were systematically studied using various biological assays, including transwell migration assay, scratch wounding assay, and tube formation assay. Biocompatibility of composite dressings was assessed in a subcutaneous implantation model, while their potential for wound healing was discerned by implantation in a full-thickness excisional defect model.

Materials and Methods

Materials

Hexadecyltrimethylammonium bromide (CTAB), tetraethyl orthosilicate (TEOS), and strontium chloride ($SrCl_2 \cdot 6H_2O$) were purchased from Sigma-Aldrich (St Louis, MO, USA). Poly (lactic-co-glycolic acid) (PLGA, 75:25 moL/moL, M*w* = 70–110 kDa) was purchased from Daigang Bioengineering Co., Ltd. (Jinan, China). Gelatin (Gel, type B, 48,722–500G-F) was obtained from Sigma-Aldrich (Shanghai, China). HUVECs and NIH-3T3 fibroblasts were purchased from the Typical Culture Collection Committee Cell Bank, Chinese Academy of Sciences (Shanghai, China). The rabbit whole blood (code # SBJ-AC-RAB03-50mL; supplemented with 10% sodium citrate) was purchased from SenBeiJia Biological Technology Co., Ltd. (Nanjing, China). The Matrigel™ (code # 356,234) was acquired from BD Biosciences (Franklin Lakes, NJ, USA). The wound dressings made from biocellulose were bought from Shandong Namet Biotechnology Co., Ltd (Jinan, China). The rest of the chemicals used were of analytical grade and were not purified any further.

Fabrication of Electrospun Membranes

Synthesis of Mesoporous Silicon with Strontium

The PSi and PSiSr were synthesized by a template method according to the previous research.[11] Briefly, TEOS (2 mL) was drop wise added into deionized water (192 mL) containing CTAB (0.4 g) and sodium hydroxide (NaOH) (0.112 g) under stirring at 80 °C for 5 h. The precipitates were collected by centrifugation, washed with deionized water and methanol and were then lyophilized and calcined at 550 °C for 5 h to afford PG@PSi particles. The PG@PSiSr particles were synthesized using similar method with 0.1g/mL of $SrCl_2 \cdot 6H_2O$.

Preparation of Membranes

The PLGA (0.7 g) and Gel (0.3 g) were dissolved into 10 mL of HFIP to afford PLGA/Gel solution (PG). The PSi (10 mg) or PSiSr (10 mg) were dispersed into a total 10 mL of PG solution to afford PG@PSi and PG@PSiSr, respectively. The PG, PG@PSi, or PG@PSiSr membranes were fabricated using electrospinning following our previous report with slight modifications.[1] Membranes were collected using a rotating mandrel (120 rotations per minute, rpm) at an applied voltage of 15 kV and spinneret-to-collector distance of 10 cm.

Physicochemical Characterization

Morphological Analysis

The TEM (JEM-2100, JEOL, Japan) was used to discern the morphology of PSiSr particles as well as PG@PSiSr membranes. Surface morphology of various samples was analyzed by SEM (Hitachi, TM-1000, Japan) with an ESM spectrometer. Energy-dispersive X-ray spectroscopy (EDS) analysis for various elements, including carbon (C), nitrogen (N), oxygen (O), Si, and Sr, was performed using SEM (SEM, Hitachi, TM-1000, Tokyo, Japan) with an EDX spectrometer after gold-sputtering of the sample (10 mA, 45s).

Structural Analysis

For structural elucidation of PSiSr particles, X-ray photoelectron spectroscopy (XPS, Kratos Analytical Ltd., Manchester, UK) was utilized to analyze samples (10 mg). The size distribution of PSiSr particles was measured using dynamic light scattering (DLS) with the assistance of a BI-200SM multi-angle dynamic/static laser scattering instrument (Brookhaven Instruments Corporation, NY, USA).

Pore Size Distribution and Cumulative pH

Pore size distribution of membranes was assessed by CFP-1100-AI capillary flow porometer (PMI Porous Materials Inc., Ithaca, NY, USA). For pH variation, samples (weight, ca. 0.5 g) were put into a centrifuge tube containing 30 mL of PBS for 21 days at 37 °C and 120 rpm. A digital pH meter (PHS3E, Leici, Shanghai, China) was used to measure the pH of the solution.

Biocompatibility and Biofunction of Membranes in vitro

Cytocompatibility

NIH-3T3 fibroblasts were cultured in DMEM supplemented with 100 U/mL penicillin, 0.1 mg/mL streptomycin, and 10% FBS in an incubator at 37 °C and 5% CO_2. For cytocompatibility assay, NIH-3T3 fibroblasts (1×10^4 cells per well) and 0.5 mL of extract solution obtained from various membranes were seeded into a 48-well cell culture plate. Cell proliferation was studies using cell counting kit (CCK-8) assay and the absorbance at 450 nm was recorded using a microplate reader (Thermo Fisher Multiskan FC, Thermo Fisher Scientific, Waltham, MA, USA). Live/dead staining was performed using live/dead assay kit (MesGen Biotechnology, Shanghai, China). To obtain the extract solution, PG, PG@PSi, and PG@PSiSr membranes (weight, ca. 10 mg) were incubated into 10 mL of culture medium for up to 24 h. The extract solution was filtered using a 0.22 μm filter paper.

The hemolysis assay was used to delineate the hemocompatibility of membranes following a previous report.[8] Briefly, 10 mL of rabbit whole blood was centrifuged at 3,000 rpm for 10 min to obtain red blood cells (RBCs). The RBCs pellet was diluted with PBS to afford 2% (v/v) cell suspension. Membranes and 1 mL of RBCs suspension were placed into a tube and incubated at 37 °C for 2 h. Cell suspension was collected from each tube and centrifuged at 3,000 rpm for 10

min and the absorbance was measured at 540 nm using a microplate reader (Thermo Fisher Multiskan FC, Thermo Fisher Scientific, Waltham, MA, USA). Deionized water and normal saline were used as positive and negative controls and their absorbance was represented as A_p and A_n, respectively, while A_s represents the absorbance of sample. Hemolysis rate was calculated by Eq. 1.

$$\text{Hemolysis rate}(\%) = \frac{(A_s - A_n)}{(A_p - A_n)} \times 100\% \quad (1)$$

Transwell Migration Assay

The chemotaxis of NIH-3T3 fibroblasts and HUVECs was studied to discern the influence of Si^{4+} and Sr^{2+} on cell migration in vitro. Electrospun membranes along with serum-free medium (~500 μL) were added into the wells in a 24-well cell culture plate. Cell suspension (2×10^4 cells per well) was added into the inserts along with the medium and incubated at 37 °C with 5% CO_2 for 12 h. Finally, inserts were carefully washed with PBS three times and the cells were fixed with 4% PFA and permeabilized with cold methanol. The permeabilized cells were stained with crystal violet. The cells on the upper side were carefully wiped, while those migrated towards lower side were observed using an optical microscope (Eclipse TS100, Nikon, Japan).

Scratch Wound Healing Assay

The chemotactic ability of Si^{4+} and Sr^{2+} for NIH-3T3 fibroblasts and HUVECs was further discerned using scratch wound healing assay in vitro. Cells (1×10^5 cells per well) were added into a 24-well cell culture plate and cultured for up to 12 h until a cell monolayer was established. The scratch on the confluent cell monolayer was produced using a 200 μL pipette tip. Afterwards, 2 mL of low-serum (supplemented with 2% FBS) medium containing extract solution of various membranes was added into the wells and they were cultured for up to 24 h. The cells were observed using an optical microscope (Eclipse TS100, Nikon, Japan). The migration ratio was determined using Eq. 2.

$$\text{Migration ratio} = \frac{(B_0 - B_1)}{B_0} \times 100\% \quad (2)$$

Where B_0 and B_1 represent the wound area at $t = 0$ and $t = 24$ h, respectively.

Tube Formation Assay

The tube formation assay was performed using HUVECs. Briefly, 100 μL pre-cooled Matrigel™ was added into a 96-well cell culture plate and incubated at 37 °C, 5% CO_2 for up to 30 min. Cell suspension (1×10^4 cells per well) and 200 μL of extract solution obtained from various membranes were added into Matrigel™ for 6 h. Angiogenic networks of HUVECs were discerned using an optical microscope (DP72, Olympus, Japan). Image J (National Institutes of Health, v1.8.0, USA) was used to quantify various angiogenic parameters, including the number of tubes.

In vivo Experiments

All in vivo experiments were adhered to the National Institutes of Health (NIH) Guide for the Care and Use of Laboratory Animals, and approved by the animal care committee of Shandong Provincial Hospital Affiliated to Shandong First Medical University, Shandong, China (No.2023–147).

Subcutaneous Implantation of Membranes

To assess the preliminary biocompatibility in vivo, the PG, PG@PSi, and PG@PSiSr membranes were transplanted into the male Sprague-Dawley (SD) rats for 28 days. Briefly, SD rats were anesthetized using an intraperitoneal (i.p.) injection of 10 wt% tribromoethanol (300 $mg \cdot kg^{-1}$). A longitudinal incision was established on the dorsal side of the rats and membranes were subcutaneously transplanted. After day 28, rats were euthanized using an overdose of tribromoethanol, and the membranes along with their surrounding tissues were explanted. Main organs, such as heart, liver, spleen, lung, and kidney were also harvested at day 28 and processed for hematoxylin and eosin (H&E) staining. On the other hand, explanted membranes were subjected to H&E staining and Masson's trichrome (MT) staining.

Wound Healing in vivo

The punch wound model was used to establish full-thickness wound defects in rats. Thirty male SD rats (weight = 190–210 g and age = 6 weeks) were randomly divided into five groups to receive control (gauze), p-control (commercial dressing), PG, PG@PSi, and PG@PSiSr. The scaffolds were replaced every three days to prevent tissue adhesion while maintaining the sustained release of therapeutic ions. Digital images of wounds were captured at different time points for up to 14 days (eg, day 0, 4, 7, 10, 14, etc). Image J was used to quantify wound length as well as wound area. The calculation of the wound closure rate involved expressing it as a percentage of the original wound area using the following Eq. 3.

$$\text{Wound closure rate} = \frac{C_t}{C_0} \times 100\% \quad (3)$$

where C_0 and C_t represent the wound areas at day 0 and other respective timepoints, respectively.

The repaired skin tissues at the defect site were harvested along with their surrounding tissues, rinsed in PBS, and fixed. Samples were embedded in paraffin and sectioned into 5 μm thick slices for histological analysis using H&E and MT staining.

Statistical Analysis

Data were reported as means ± standard deviation (SD) and the statistical analysis involved using one-way analysis of variance (ANOVA) followed by Tukey's multiple comparison test. The detailed statistical analysis information was placed in Supplementary Information (Table S1–S22).

Results

Characterizations of Electrospun Membranes

To incorporate strontium (Sr) into electrospun membranes, we fabricated PSiSr particles. The PSiSr particles displayed spherical shape with an average size of 217.4 ± 0.07 nm as measured by DLS (Figure 1a and d). These PSiSr particles were loaded into electrospun fibers; the latter showed a uniform and smooth surface morphology, which is indicative of the successful incorporation of the synthesized particles into fibers (Figure 1b, Figure S1, Supplementary Information). TEM also confirmed the successful incorporation of particles into fibers (Figure 1b). We also fabricated electrospun fibers with or without the loading of PSi or PSiSr. Average fiber diameter was found to be 0.21 ± 0.07 μm, 0.25 ± 0.04 μm, and 0.29 ± 0.05 μm for PG, PG@PSi, and PG@PSiSr groups, respectively (Figure 1e–g). These results confirmed the successful incorporation of PSi and PSiSr into fibers. The EDS mapping revealed successful synthesis of PSiSr particles (Figure 1c). Elemental percentage of C, O, N, Si, and Sr was 57.0%, 31.4%, 9.8%, 0.8%, and 0.1%, respectively (Figure 1i). XPS analysis revealed that the content of Si and Sr were 14.13% and 0.06% in the PSiSr particles (Figure 1h).

Electrospun membranes were also evaluated for the porosity and water uptake. The porosity of PG, PG@PSi, and PG@PSiSr membranes was 55.3 ± 0.7%, 53.2 ± 1.5%, and 51.3 ± 1.3%, while the water absorption ratio was 839.7 ± 27.5%, 687.0 ± 50.0%, 652.3 ± 57.2%, respectively (Figure S2, S3, Supplementary Information). The pore size of the membranes was in a range of 0.8–2.0 μm (Figure 1j). Since the degradation of membranes may cause a reduction in the pH of the surrounding tissue microenvironment, we incubated membranes in PBS and measured the pH of the supernatant. There was a significant difference among various groups in terms of the change in the pH (7.40 ± 0.04, 7.60 ± 0.06, 7.73 ± 0.03 for PG, PG@PSi, and PG@PSiSr membranes, respectively) (Figure 1k).

The release of Si^{4+} and Sr^{2+} from membranes was measured for up to 192 h. The PG@PSiSr displayed the sustained release of therapeutics ions. The concentration of Si^{4+} and Sr^{2+} was found to be 2688 ppm and 887 ppm at 192 h, respectively (Figure S4, Supplementary Information). The swelling rate was found to be 21.6 ± 2.6%, 10.8 ± 1.7%, and 14.6 ± 1.4% at 72h for PG, PG@PSi, and PG@PSiSr membranes, respectively. These results indicated that the PSi and PSiSr could attenuate the swelling rate of scaffolds (Figure S5a, Supplementary Information). The residual weight of the scaffolds was found to be 45.2 ± 3.9%, 34.0 ± 4.0%, and 39.4 ± 2.8% at day 21 for PG, PG@PSi and PG@PSiSr membranes, respectively, which manifested that the inorganic NPs impeded the swelling of scaffolds (Figure S5b, S6,

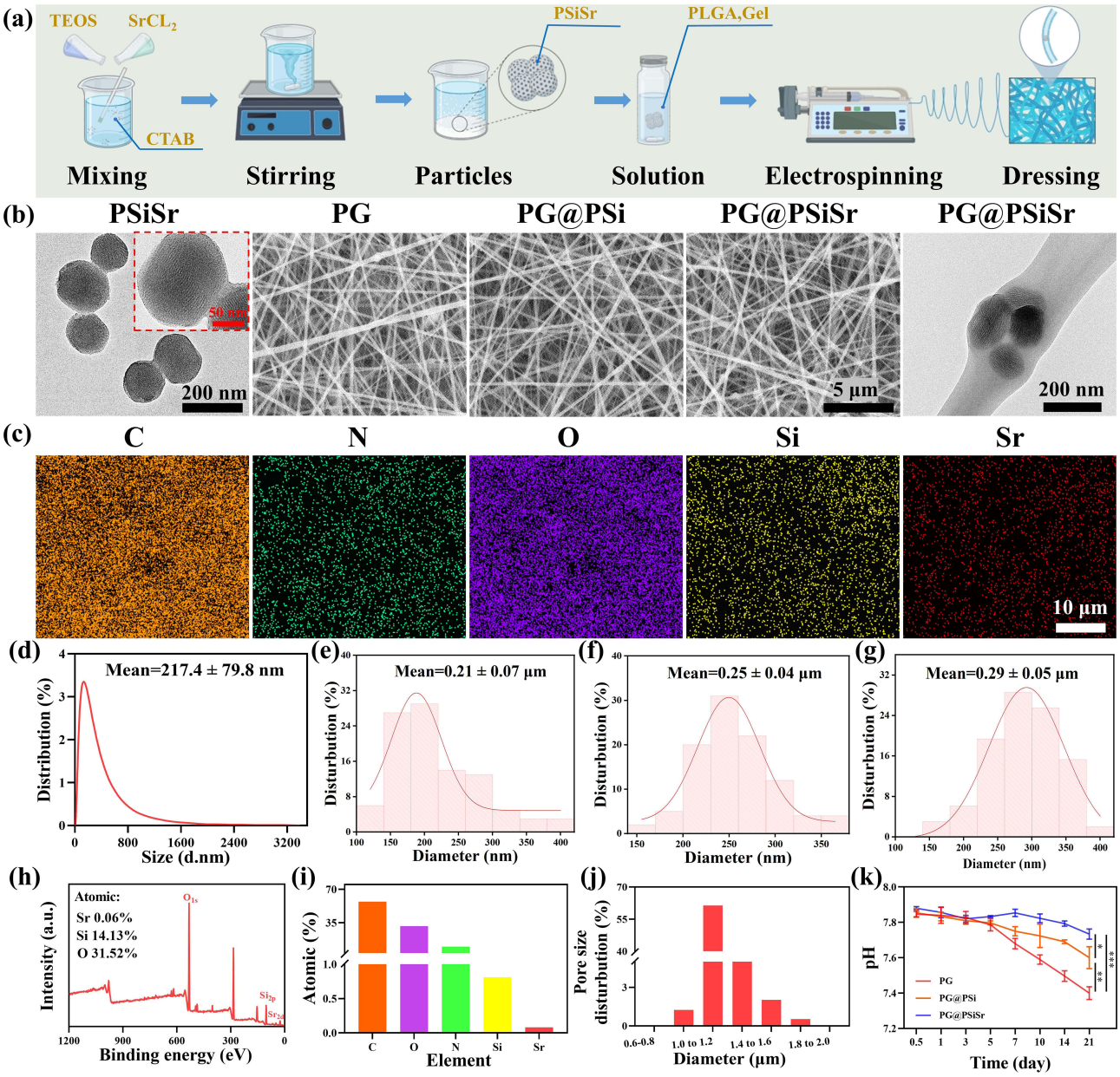

Figure 1 Characterization of the scaffolds.

Notes: (**a**) Schematic illustration of the synthesis of PSiSr particles as well as their corresponding membranes by electrospinning. (**b**) The TEM of PSiSr particles, SEM of membranes, and TEM of PG@PSiSr fiber. (**c**) EDS analysis of PG@PSiSr membrane. (**d**) Diameter distribution of PSiSr particles. Diameter distribution of PG (**e**), PG@PSi (**f**), and PG@PSiSr (**g**). (**h**) XPS spectra of PSiSr particles. (**i**) EDS of PG@PSiSr membrane. (**j**) The pore size distribution of the PG@PSiSr membrane. (**k**) Cumulative pH at different time points of the incorporation of PG, PG@PSi, and PG@PSiSr membranes in the PBS (n=3). *P < 0.05, **P < 0.01, and ***P < 0.001.

Supplementary Information). The PG@PSiSr manifested a more rapid degradation than that of PG@PSi, which is ascribed to an increase in the solubility of the PSi particles with the incorporation of Sr.

Biocompatibility and Biofunction of Membranes in vitro

The hemostatic ability of membranes was next ascertained. While the supernatants collected from the negative groups as well as PG, PG@PSi, and PG@PSiSr manifested slight yellowish colour in a hemolysis assay, the positive group exhibited an intense red colour; the latter is indicative of significant hemolysis (Figure 2a). Hemolysis rate of all of the membrane was found to be less than 2% (PG = 0.59 ± 0.63%, PG@PSi = 1.20 ± 0.59%, and PG@PSiSr = 1.20 ± 0.74%), which is indicative of negligible hemolysis (Figure 2d).[1]

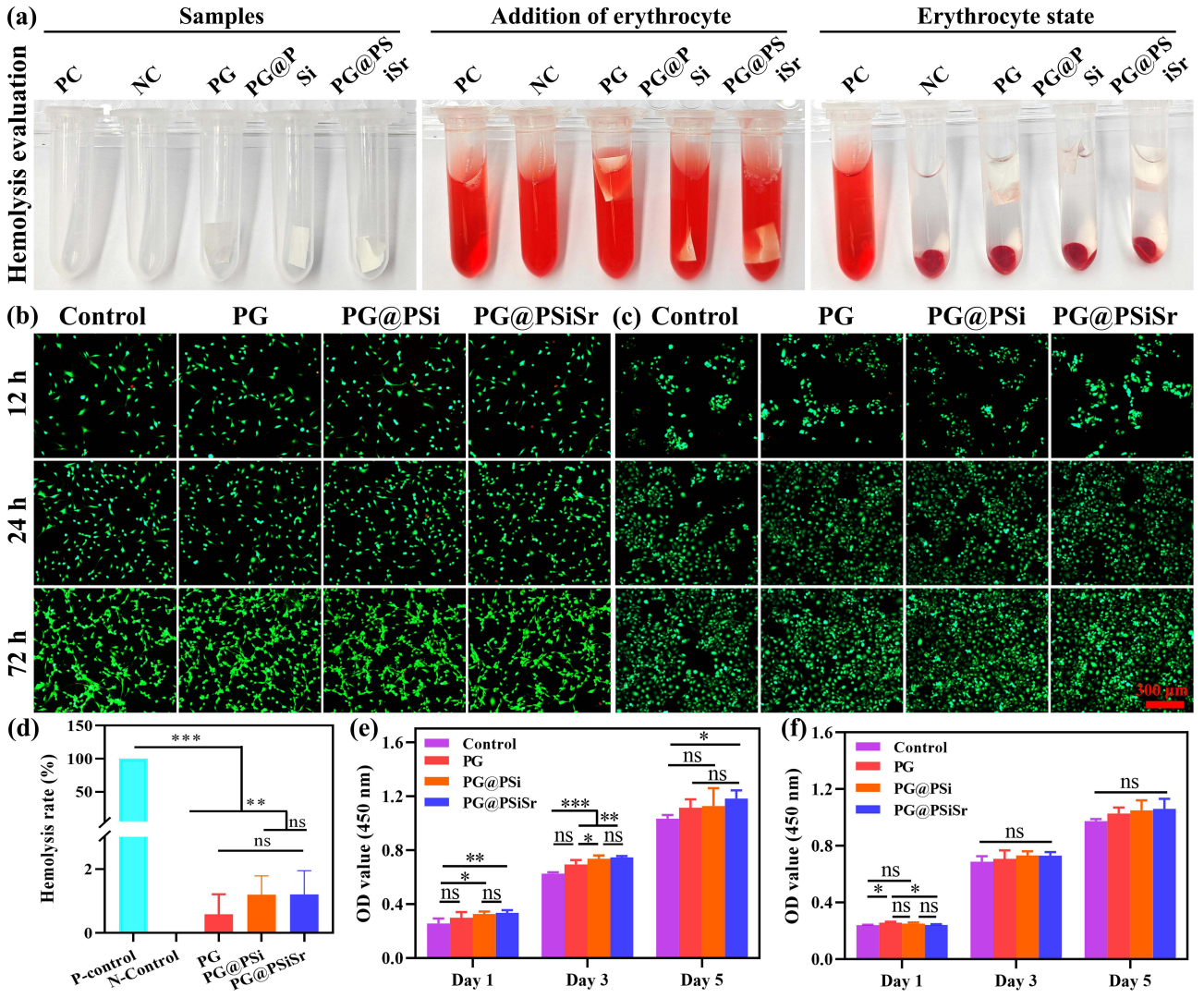

Figure 2 Cytocompatibility and hemocompatibility assay of samples in vitro.
Notes: (**a**) A hemolytic activity assay process (n=6). Live/dead staining of NIH-3T3 fibroblasts (**b**) and HUVECs (**c**) at 12 h, 24 h and 72 h after incubation with the extract solution of various membranes. Quantitative analysis of the hemolysis rate (**d**), proliferation of NIH-3T3 fibroblasts (**e**) (n=5) and HUVECs (**f**) (n=4). The "ns" means no significant difference among the groups, *P < 0.05, **P < 0.01, and ***P < 0.001.

NIH-3T3 fibroblasts and HUVECs were used to discern the biocompatibility of membranes in vivo using live/dead staining and CCK-8 assay. As can be seen from Figure 2b and c, most of the seeded cells survived well (green colour indicates live cells) with only a few dead cells (red colour indicates the dead cells) once cultured along with the extract solution of various membranes for up to 72 h in vitro. The density of live cells was increased with an increase in the culture time in all groups as discerned with the higher fluorescence (Figure 2b). Moreover, cells in all groups showed good proliferation over a time point of 5 days in vitro. These results showed that the prepared membranes were cytocompatible without any obvious cell cytotoxicity (Figure 2e–f).

Since therapeutic ions, including Si^{4+} and Sr^{2+} may influence cell migration, the extract solution of various membranes was utilized in a transwell migration assay, the migration of HUVECs and NIH-3T3 fibroblasts was evaluated (Figure 3a).[12] The PG@PSi and PG@PSiSr groups showed a significant chemotactic effect and recruited more cells as compared to the PG and control groups (Figure 3b). The incorporation of Sr did not increase cell migration, which is indicative of its negligible effect on cell migration (migration of HUVECs: control = 18.7 ± 5.5/HPF, PG = 38.3 ± 7.2/HPF, PG@PSi = 47.0 ± 6.1/HPF, and PG@PSiSr = 67.0 ± 11.5/HPF; migration of NIH-3T3 fibroblasts: control = 3.7 ± 1.5/HPF, PG = 17.7 ± 5.1/HPF, PG@PSi = 47.7 ± 2.5/HPF, PG@PSiSr = 51.7 ± 2.5/HPF) (Figure 3e–f).

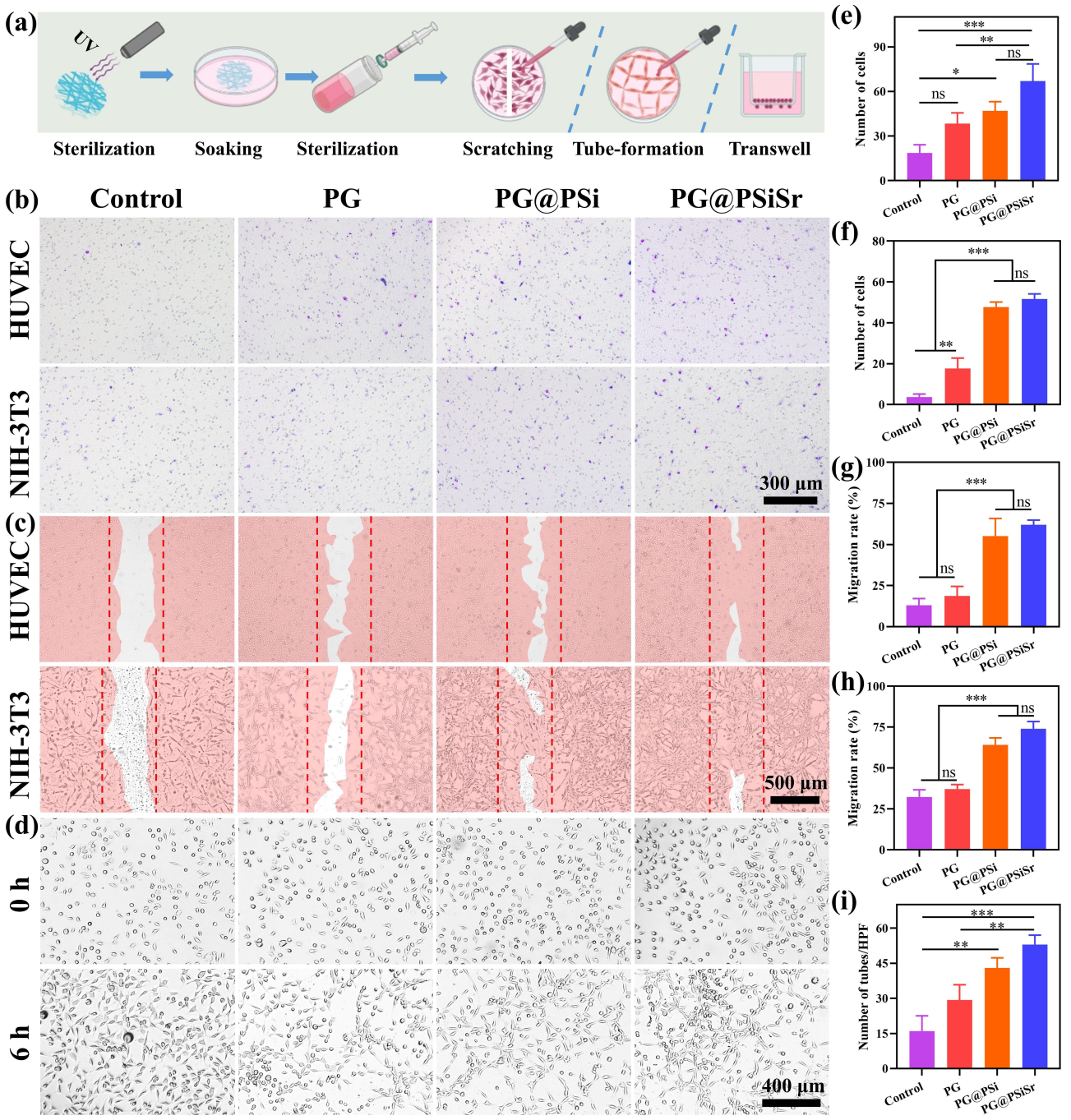

Figure 3 Biological functions of samples in vitro.

Notes: (**a**) Schematic diagram of different experimental procedure. (**b**) Transwell migration assay and (**c**) scratch wound healing assay of HUVECs and NIH-3T3 fibroblasts. (**d**) Formation of the tubule-like networks of HUVECs in vitro. Quantitative analysis of the number of migrated cells in a transwell migration assay (**e** and **f**, n=3), migration ratio of HUVECs and NIH-3T3 fibroblasts in a scratch wound healing assay (**g** and **h**, n=3), the number of tubes in tubule-like network formation assay of HUVECs in vitro (**i**, n=3). The "ns" means no significant difference among the groups, *P < 0.05, **P < 0.01, and ***P < 0.001.

Scratch wound healing assay was also performed to delineate the effect of various groups on cell migration in vitro. Among all groups, PG@PSi and PG@PSiSr groups showed significantly higher migration of HUVECs and NIH-3T3 fibroblasts. (migration of HUVECs: control = 13.0 ± 4.1%, PG = 18.7 ± 5.9%, PG@PSi = 55.1 ± 6.8%, and PG@PSiSr = 62.0 ± 2.9%; migration of NIH-3T3 fibroblasts: control = 32.3 ± 4.4%, PG = 37.1 ± 2.8%, PG@PSi, 64.2 ± 4.2%, PG@PSiSr = 74.0 ± 4.4%) (Figure 3c, g and h). Higher cell migration was ascribed to the release of Si^{4+}, which may also have implications for tissue repair in vivo.

The Si^{4+} and Sr^{2+} have been incorporated into bioactive glasses (BGs) owing to their stimulatory effects on vasculogenesis and osteogenesis.[7,13] Angiogenic effects of the membranes were therefore discerned using an in vitro tube formation assay of HUVECs. The PG@PSi and PG@PSiSr exhibited significantly more tubes than that of the control and PG groups (control, 16.0 ± 6.6/HPF, PG, 29.3 ± 6.5/HPF, PG@PSi, 43.0 ± 4.4/HPF, and PG@PSiSr, 53.0 ± 4.0/HPF) (Figure 3i). Similarly, PG@PSi and PG@PSiSr groups manifested significantly more capillary-like networks at 6 h in vitro (Figure 3d).

Biocompatibility of Membranes in vivo

For the preliminary biocompatibility of scaffolds in vivo, they were subcutaneously implanted in rats for up to 4 weeks (Figure 4a). H&E staining revealed that all of the membranes could support cellular infiltration as early as 2 weeks along with a few more numbers of inflammatory cells in PG@PSi and PG@PSiSr groups than that in the PG group (Figure 4b, Figure S7a, Supplementary Information). The explants harvested at 4 weeks post-operatively showed voids with cellular clusters (Figure 4c). The numbers of inflammatory cells in the PG@PSiSr group were significantly lower than that of the PG group, which further indicated that PSiSr had certain anti-inflammatory properties (Figure S7a, Supplementary Information).

The MT staining showed relatively less collagen deposition in all groups by 2 weeks, which was substantially increased after 4 weeks (Figure 4b and c). Meanwhile, the number of fibroblasts were larger in the PG@PSi and PG@PSiSr groups than that in PG group at 2 weeks (Figure S7b, Supplementary Information). Especially, we observed wide bundles of collagen fiber production in PG@PSiSr group 4 weeks post-operatively, which indicated the production

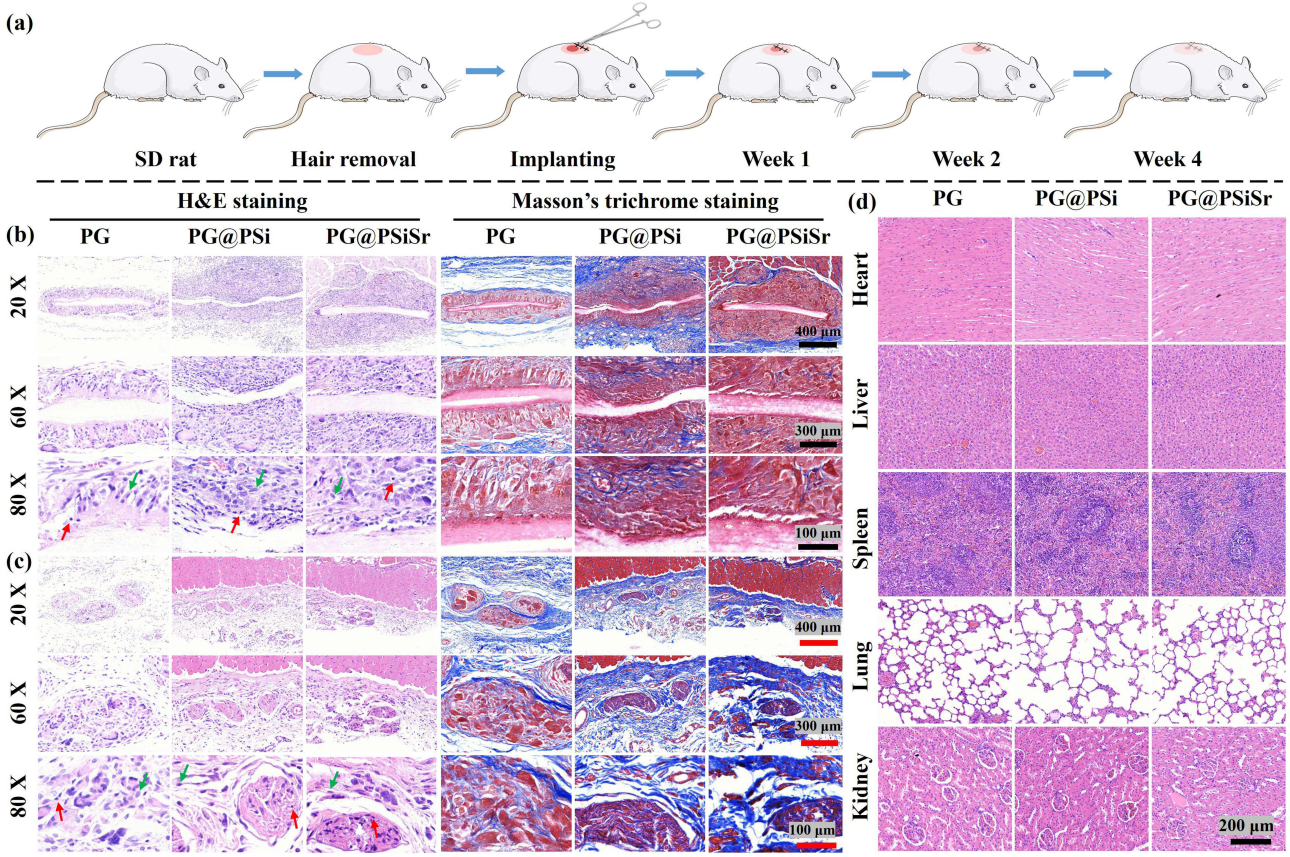

Figure 4 Preliminary biocompatibility of membranes in a subcutaneous implantation model in rats.
Notes: (**a**) Schematic diagram of subcutaneous implantation of membranes for up to 4 weeks. H&E staining and Masson's trichrome staining of explanted membranes as well as adjacent tissues after 2 weeks (**b**) and 4 weeks (**c**). (**d**) H&E staining of main organs collected from the animals after 4 weeks. Red and green arrows indicating inflammatory cells and fibroblasts.

of mature collagen (Figure 4c). Histological analysis of main organs also did not show an obvious toxicity and lesions, which was indicative of the safety of the scaffolds (Figure 4d).

Wound Healing in vivo

To delineate the potential of scaffolds for skin regeneration, they were transplanted into the full-thickness excisional skin defects in SD rats. Dressings were replaced every three days and wounds were photographed 2 weeks post-operatively (Figure 5a). The skin defects were gradually healed as the implantation time progressed (Figure 5b). The residual wound area was significantly less in PG@PSi and PG@PSiSr groups 14 days post-operatively, which is indicative of an accelerated wound repair (Figure 5e). The wound healing ratio was 71.7 ± 2.7%, 79.5 ± 7.5%, 87.6 ± 5.1%, 92.2 ±

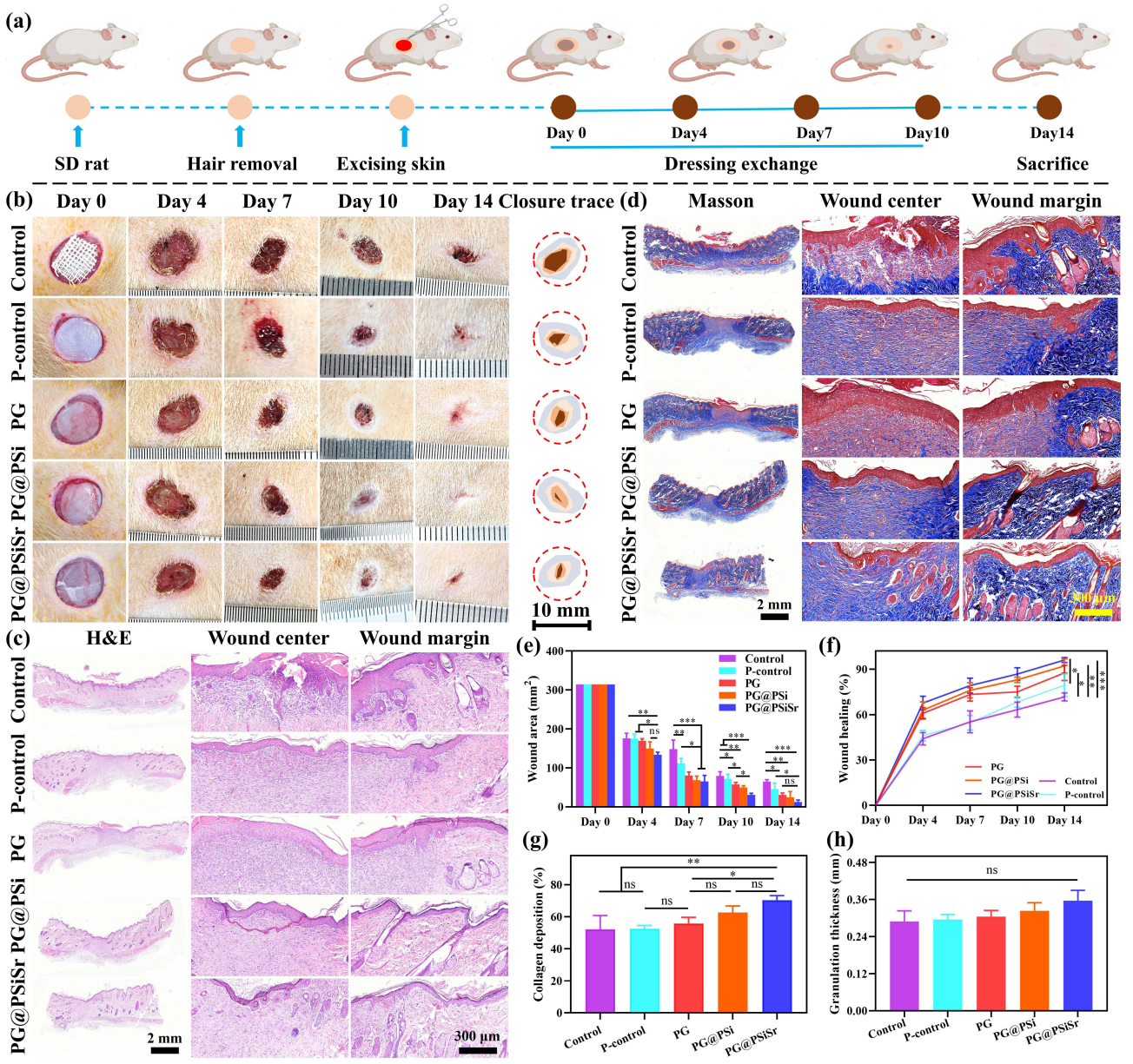

Figure 5 Implantation of electrospun membranes in a full-thickness excisional defect model in rats.

Notes: (**a**) Schematic illustration showing the preparation of incision site and implantation of membranes. (**b**) Representative images of wound size and closure trace of wounds for up to 14 days. The H&E staining (**c**) and MT staining (**d**) of wound site at day 14 post-operatively. Wound area at different time points normalized with respect to day 0 (**e**, n=3). Wound healing was increased concomitantly as the implantation time was increased (**f**, n=3). Collagen deposition (**g**, n=3) and thickness of the granulation tissues (**h**, n=3) of wound site at day 14. The "ns" means no significant difference among the groups, *P < 0.05, **P < 0.01, and ***P < 0.001.

4.7%, and 96.1 ± 1.7% for control, P-control, PG, PG@PSi, and PG@PSiSr group, respectively (Figure 5f). It is worthy to note that the PG@PSi and PG@PSiSr groups showed significantly better skin repair than the P-control (Figure 5b).

The repaired skin as well as adjacent tissues were harvested and subjected to histological analysis. H&E staining showed unhealed full-thickness skin defects alongside residual visible scabs in the control group. In contrast, all other groups showed an obvious de novo production of epithelial cell layer (Figure 5c). The PG@PSi and PG@PSiSr groups also showed a mild inflammation alongside the formation of skin appendages (eg, sweat glands, hair follicles, etc.), especially, at the wound margin as compared to the other groups (Figure 5c). MT staining further indicated an accumulation and maturation of collagen in the defect site in PG@PSi and PG@PSiSr groups by day 14 post-operatively (Figure 5d). The percentage of collagen deposition was 52.0 ± 8.7%, 52.5 ± 2.1%, 55.8 ± 3.8%, 62.6 ± 4.1%, and 70.3 ± 2.9% for control, P-control, PG, PG@PSi, and PG@PSiSr group, respectively (Figure 5g). Interestingly, the PG@PSiSr seemed to display the thicker granulation tissues than that of other groups in wound site (Figure 5h).

Moreover, the Western blot showed the PG@PSiSr group possessed higher protein expression than the other groups in terms of CD31 and Col-I, while the lower protein expression of IL-6 and MMP-9 (Figure S8, Supplementary Information). These results showed that the PSi and PSiSr could significantly facilitate wound repair alongside ECM production.

Discussion

The skin injuries often occur following deep trauma, severe burn injury, or surgical incision, which lead to the loss of skin function and also possibly perturb natural repair process due to inflammation burden and tactile dysfunction.[14] While skin manifests intrinsic repair capability, poor skin wound management may possibly cause hypertrophic scarring and even chronic wounds, thereby negatively impacting the QOL.[15,16] This necessitates the advent of functional dressing to promote rapid wound closure and healing for a functional tissue reconstruction.[17] Generally, wound repair is a dynamic process, which involves multiple sequential healing events, including homeostasis, inflammatory cell recruitment, ECM deposition, and re-epithelialization.[18] Inflammation regulation and vascular network induction, especially, are very important owing to their diverse implications for the subsequent functional skin repair and revascularization.[19] Traditionally, therapeutics and GFs are incorporated into natural or synthetic polymer-based scaffolds or ECM-based wound dressings. Alternatively, the NMs, such as BGs and therapeutic metal ions have also been shown to stimulate vascularization and de novo skin reconstruction.[1,20] In this study, we fabricated composite wound dressings by loading

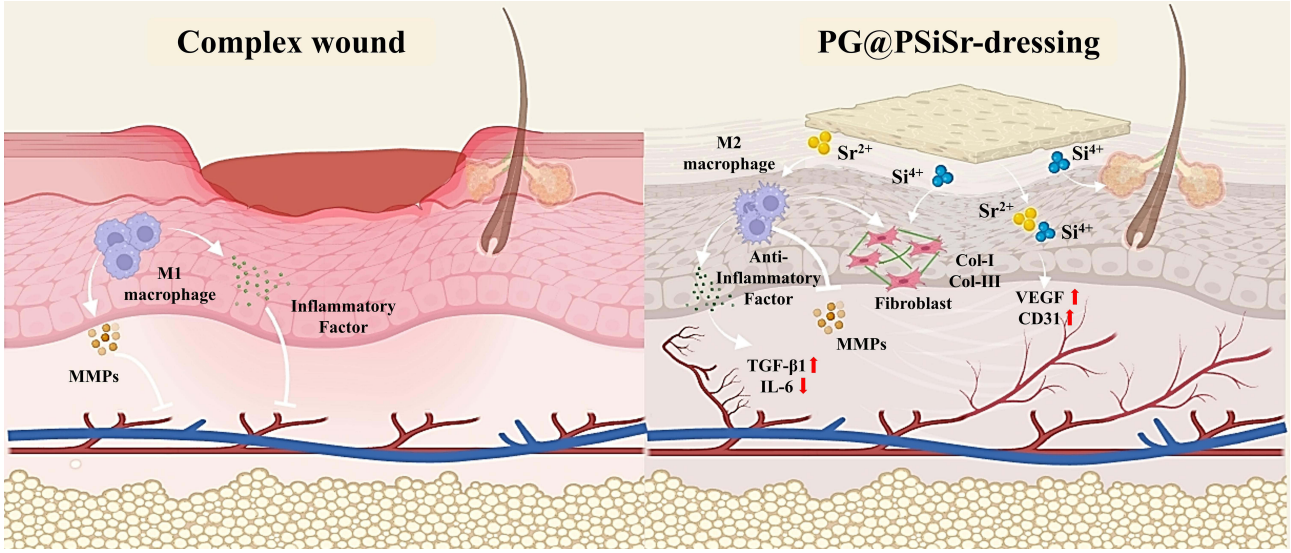

Figure 6 Schematic illustration of the mechanism of improved wound healing by PG@PSiSr dressings.

in-house synthesized mesoporous silicon and strontium-loaded mesoporous silicon, namely PSi and PSiSr, respectively (Figure 6).

While Si can stimulate the formation of angiogenic networks as well as increase cell growth and metabolic processes, Sr could facilitate angiogenesis via inflammation resolution at the healing site.[21,22] The PSi particles possess an affinity for the moisture, which may increase water uptake and hydrolytic degradation for the sustained release of Si^{4+}.[7,23] The Sr^{2+} can be effectively loaded into the porous network of PSi due to porosity of the latter.[7,24] Therefore, we successfully synthesized PSi as well as its Sr-substituted counterpart (PSiSr). These particles were next incorporated into PLGA/Gel-based electrospun fibers for the localized delivery at the defect site.

Electrospun fibers are widely employed as substrates for cell culture as well as depots for the localized release of therapeutics and biologics for tissue repair, thanks to their high surface-to-volume ratio, ECM-reminiscent microstructure and porous morphology.[25] These fibrous dressings may further isolate the wound site from the external environment to shield microorganisms, absorb tissue exudates, and permit the diffusion of oxygen and the transport of nutrients.[26] The PSi and PSiSr particles displayed diameter (ca. 200 nm), while the electrospun fibers possessed a diameter of 150–500 nm, thereby providing the basis for particles to be loaded into fibers to afford fibrous dressings.[27]

The PG@PSiSr dressings displayed negligible hemolysis rate and supported cell growth, thereby showing cyto-compatibility. The biocompatibility of these fibers may also be ascribed to the PLGA and gelatin, which are biocompatible and biodegradable and have been intensively studied for tissue repair.[28] While dressings containing PSi and PSiSr did not manifest distinct improvement in cell viability and cell proliferation than that of PG, they exhibited distinct effect on the chemotaxis of NIH-3T3 fibroblasts and HUVECs as well as angiogenic network formation of HUVECs as revealed by different types of in vitro assays, such as transwell migration assay, scratch wounding assay, and tube formation assay.

Since PG@PSiSr dressings can release therapeutic ions, such as Sr^{2+} and Si^{4+}, and may increase the pH at the implantation site, we initially evaluated the pH of the supernatants collected after the degradation of membranes for up to a certain time point and subsequently performed subcutaneous implantation to further probe the biocompatibility.[29] The PG@PSiSr dressings encouraged host cell infiltration as well as promoted the deposition of collagen for a constructive remodeling.[30]

Previously, Si-based BGs were shown to facilitate angiogenesis via an upregulation of VEGF as well as promote collagen production and re-epithelialization by enriching angiogenic genes, such as fibroblast growth factor (FGF), epidermal growth factor (EGF), and collagen type 1 (Col-I) (Figure 6).[31,32] Since the lack of blood vessels and prolonged inflammatory phase may adversely influence constructive wound repair, we next discerned angiogenic and reparative effects of membranes in a full-thickness excisional defect model in rats.

The Sr element could stimulate the expression of the VEGF by regulating the Wnt signaling pathway, bFGF by stimulating the expression of FGF receptors, and stimulate the proliferation and migration of ECs, which may promote vascularization and modulate inflammation (Figure 6).[33,34] We observed rapid wound closure alongside skin appendages formation in PG@PSiSr dressings than that in the other groups. It is anticipated that the loaded therapeutic ions may play a supportive role in promoting wound repair.

There are also several limitations of this study. We only carried out histological analysis to confirm the wound closure. An in-depth analysis of the tissue exudate using proteomics and transcriptomics as well as further screening of the harvested tissues with immunohistochemical techniques may provide a new mechanistic insight on the developed dressings. Similarly, we did not evaluate the production of GFs at the injury site. Since localized release of Sr^{2+} and Si^{4+} ions can stimulate the production of the GFs as well as the synthesis of key regulatory proteins, a further analysis is warranted.

Conclusion

We successfully fabricated PSiSr particles and prepared PG@PSiSr dressings using electrospinning. The PG@PSi and PG@PSiSr dressings showed cytocompatibility as well as promoted the migration of fibroblasts and endothelial cells (ECs) in multiple in vitro screening assays, including transwell migration assay, scratch wounding assay, and tube formation assay. Preliminary biocompatibility evaluation in a subcutaneous implantation model revealed the significant

promise of the dressings to promote host cell infiltration as well as collagen production. On the other hand, the application of dressings in a full-thickness excisional defect model facilitated rapid wound closure and mild inflammation in PG@PSiSr dressings. Taken together, these PSrSi-loaded composite dressings may be worthy for future investigations to encourage wound repair.

Funding

The part of this research was funded by Taishan Scholars Program of Shandong Province (tsqn201812141), Shandong Provincial Natural Science Foundation (ZR2021MH004, ZR2022QH063), Academic promotion program of Shandong First Medical University (2019RC016).

Disclosure

The authors declare that they have no known competing financial interests or personal relationships that could have appeared to influence the work reported in this paper.

References

1. Yuan Z, Zhang L, Jiang S, et al. Smart Materials in Medicine nano fibrous dressing enables scarless wound healing. *Smart Mater Med*. 2023;4:407–426. doi:10.1016/j.smaim.2023.01.001
2. Yuan Z, Zhao Y, Shafiq M, et al. Multi - Functional fibrous dressings for burn injury treatment with pain and swelling relief and scarless wound healing. *Adv Fiber Mater*. 2023;5(6):1963–1985. doi:10.1007/s42765-023-00320-5
3. Teng L, Shao Z, Bai Q, et al. Biomimetic glycopolypeptide hydrogels with tunable adhesion and microporous structure for fast hemostasis and highly efficient wound healing. *Adv Funct Mater*. 2021;31(43):1–11. doi:10.1002/adfm.202105628
4. Turner CT, Hasanzadeh Kafshgari M, Melville E, et al. Delivery of flightless I siRNA from porous silicon nanoparticles improves wound healing in mice. *ACS Biomater Sci Eng*. 2016;2(12):2339–2346. doi:10.1021/acsbiomaterials.6b00550
5. Zhang X, Karagöz Z, Swapnasrita S, et al. Development of mesoporous silica nanoparticle-based films with tunable arginine-glycine-aspartate peptide global density and clustering levels to study stem cell adhesion and differentiation. *ACS Appl Mater Interfaces*. 2023;15(32):38171–38184. doi:10.1021/acsami.3c04249
6. Liu M. Composite superelastic aerogel scaffolds containing flexible SiO2 nanofibers promote bone regeneration. *Adv Healthc Mater*. 2022;11:1–15 doi:10.1002/adhm.202200499.
7. Leite ÁJ, Gonçalves AI, Rodrigues MT, Gomes ME, Mano JF. Strontium-doped bioactive glass nanoparticles in osteogenic commitment. *ACS Appl Mater Interfaces*. 2018;10(27):23311–23320. doi:10.1021/acsami.8b06154
8. Yuan Z, Zhang L, Zheng H, Shafiq M, Song J. The ZnO-based fibrous poly (L -lactide-co-glycolide)/ gelatin dressings enable rapid hemostasis and skin regeneration in an infectious wound model. *J Drug Deliv Sci Technol*. 2023;89:105072. doi:10.1016/j.jddst.2023.105072
9. Cai J, Liu J, Xu J, et al. Constructing high-strength nano-micro fibrous woven scaffolds with native-like anisotropic structure and immunoregulatory function for tendon repair and regeneration. *Biofabrication*. 2023;15(2):025002. doi:10.1088/1758-5090/acb106
10. Yuan Z, Shafiq M, Zheng H, et al. Materials & Design Multi-functional fibrous dressings for infectious injury treatment with anti-adhesion wound healing. *Mater Des*. 2023;235:112459. doi:10.1016/j.matdes.2023.112459
11. Guo X, Shi H, Zhong W, et al. Tuning biodegradability and biocompatibility of mesoporous silica nanoparticles by doping strontium. *Ceram Int*. 2020;46(8):11762–11769. doi:10.1016/j.ceramint.2020.01.210
12. Hao J, Bai B, Ci Z, et al. Large-sized bone defect repair by combining a decalcified bone matrix framework and bone regeneration units based on photo-crosslinkable osteogenic microgels. *Bioact Mater*. 2022;14:97–109. doi:10.1016/j.bioactmat.2021.12.013
13. Iqbal MF, Chen Z, Zhao Y, et al. Mesoporous strontium hydroxide hydrate as a nanostructure-dependent electrocatalyst for hydrogen evolution reaction. *ACS Appl Nano Mater*. 2022;5(12):18188–18198. doi:10.1021/acsanm.2c04071
14. Zhang J, Zheng Y, Lee J, et al. A pulsatile release platform based on photo-induced imine-crosslinking hydrogel promotes scarless wound healing. *Nat Commun*. 2022;12(1):1670. doi:10.1038/s41467-021-21964-0
15. Zhang Q, Chang C, Qian C, et al. Photo-crosslinkable amniotic membrane hydrogel for skin defect healing. *Acta Biomater*. 2021;125:197–207. doi:10.1016/j.actbio.2021.02.043
16. Shi X, Chen Z, He Y, et al. Dual light-responsive cellulose nanofibril-based in situ hydrogel for drug-resistant bacteria infected wound healing. *Carbohydr Polym*. 2022;297:120042. doi:10.1016/j.carbpol.2022.120042
17. Zhong Y, Seidi F, Wang Y, et al. Injectable chitosan hydrogels tailored with antibacterial and antioxidant dual functions for regenerative wound healing. *Carbohydr Polym*. 2022;298:120103. doi:10.1016/j.carbpol.2022.120103
18. Jia Z, Gong J, Zeng Y, et al. Bioinspired conductive silk microfiber integrated bioelectronic for diagnosis and wound healing in diabetes. *Adv Funct Mater*. 2021;31(19):1–13. doi:10.1002/adfm.202010461
19. Wang J, Lin J, Chen L, Deng L, Cui W. Endogenous electric-field-coupled electrospun short fiber via collecting wound exudation. *Adv Mater*. 2022;34:1–15.
20. Ha Y, Ma X, Li S, et al. Bone microenvironment-mimetic scaffolds with hierarchical microstructure for enhanced vascularization and bone regeneration. *Adv Funct Mater*. 2022;2200011(20):2200011. doi:10.1002/adfm.202200011
21. Ma L, Zhou Y, Zhang Z, et al. Multifunctional bioactive Nd-Ca-Si glasses for fluorescence thermometry, photothermal therapy, and burn tissue repair. *Sci Adv*. 2020;6(32). doi:10.1126/sciadv.abb1311

22. Maleki H, Shahbazi M-A, Montes S, et al. Mechanically strong silica-silk fibroin bioaerogel: a hybrid scaffold with ordered honeycomb micromorphology and multiscale porosity for bone regeneration. *ACS Appl Mater Interfaces*. 2019;11(19):17256–17269. doi:10.1021/acsami.9b04283
23. Wu S, Zhao W, Sun M, et al. Novel bi-layered dressing patches constructed with radially-oriented nanofibrous pattern and herbal compound-loaded hydrogel for accelerated diabetic wound healing. *Appl. Mater. Today*. 2022;28:101542. doi:10.1016/j.apmt.2022.101542
24. Chen L, Deng C, Li J, et al. 3D printing of a lithium-calcium-silicate crystal bioscaffold with dual bioactivities for osteochondral interface reconstruction. *Biomaterials*. 2019;196:138–150. doi:10.1016/j.biomaterials.2018.04.005
25. Boda SK, Chen S, Chu K, Kim HJ, Xie J. Electrospraying electrospun nanofiber segments into injectable microspheres for potential cell delivery. *ACS Appl Mater Interfaces*. 2018;10(30):25069–25079. doi:10.1021/acsami.8b06386
26. Chen Y, Xu W, Shafiq M, et al. Three-dimensional porous gas-foamed electrospun nanofiber scaffold for cartilage regeneration. *J Colloid Interface Sci*. 2021;603:94–109. doi:10.1016/j.jcis.2021.06.067
27. Tang Q, Ke Q, Chen Q, et al. Flexible, breathable, and self-powered patch assembled of electrospun polymer triboelectric layers and polypyrrole-coated electrode for infected chronic wound healing. *ACS Appl Mater Interfaces*. 2023;15(14):17641–17652. doi:10.1021/acsami.3c00500
28. Ma J, Wu C. Bioactive inorganic particles-based biomaterials for skin tissue engineering. *Exploration*. 2022;2(5):20210083. doi:10.1002/EXP.20210083
29. Wu F, Yuan Z, Shafiq M, et al. Synergistic effect of glucagon-like peptide-1 analogue liraglutide and ZnO on the antibacterial, hemostatic, and wound healing properties of nanofibrous dressings. *J Biosci Bioeng*. 2022;134(3):248–258. doi:10.1016/j.jbiosc.2022.06.004
30. Liu M, Wang X, Li H, et al. Magnesium oxide-incorporated electrospun membranes inhibit bacterial infections and promote the healing process of infected wounds. *J Mater Chem B*. 2021;9(17):3727–3744. doi:10.1039/D1TB00217A
31. Ren X, Han Y, Wang J, et al. An aligned porous electrospun fibrous membrane with controlled drug delivery – an efficient strategy to accelerate diabetic wound healing with improved angiogenesis. *Acta Biomater*. 2018;70:140–153. doi:10.1016/j.actbio.2018.02.010
32. Shen Y, Xu G, Huang H, et al. Sequential release of small extracellular vesicles from bilayered thiolated alginate/polyethylene glycol diacrylate hydrogels for scarless wound healing. *ACS Nano*. 2021;15(4):6352–6368. doi:10.1021/acsnano.0c07714
33. Li Z, Chen S, Wu B, et al. Multifunctional dual ionic-covalent membranes for wound healing. *ACS Biomater Sci Eng*. 2020;6(12):6949–6960. doi:10.1021/acsbiomaterials.0c01512
34. Shi Q, Luo X, Huang Z, et al. Cobalt-mediated multi-functional dressings promote bacteria-infected wound healing. *Acta Biomater*. 2019;86:465–479. doi:10.1016/j.actbio.2018.12.048